DELPHI Collaboration

DELPHI 2004-036 CONF 711
28 July, 2004

Determination of the $e^+e^- \to \gamma\gamma(\gamma)$ cross-section at LEP 2

M. Espirito-Santo, P. Gonçalves, A. Onofre, M. Pimenta and B. Tomé
LIP-IST-FCUL, Av. Elias Garcia, 14, 1, P-1000 Lisboa, Portugal

Abstract

A test of the benchmark QED process $e^+e^- \to \gamma\gamma(\gamma)$ is reported, using the data collected with the DELPHI detector at LEP 2. The data analysed were recorded at centre-of-mass energies ranging from 161 GeV to 208 GeV and correspond to a total integrated luminosity of 656.4 pb^{-1}. The Born cross-section for the process $e^+e^- \to \gamma\gamma(\gamma)$ was determined, confirming the validity of QED at the highest energies ever attained in electron-positron collisions. Lower limits on the parameters of a number of possible deviations from QED, predicted within theoretical frameworks expressing physics beyond the Standard Model, were derived.

Contributed Paper for ICHEP 2004 (Beijing)

1 Introduction

An analysis of the process $e^+e^- \to \gamma\gamma(\gamma)$ is reported. The data analysed were collected with the DELPHI detector [1] at LEP 2, at collision energies, $\sqrt{s}$, ranging from 161 GeV up to 208 GeV, corresponding to a total integrated luminosity of 656.4 pb^{-1}. The studied reaction is an almost pure QED (Quantum ElectroDynamics) process which, at orders above α^2, is mainly affected by QED corrections, such as soft and hard *bremsstrahlung* and virtual corrections, compared to which the weak corrections due to the exchange of virtual massive gauge bosons are very small [2, 3, 4]. Therefore, any significant deviation between the measured and the predicted QED cross-sections could unambiguously be interpreted as a manifestation of non-standard physics. Moreover, the differential cross-section terms expressing interferences between QED and various non-standard physics processes, behave very differently from the QED term in their dependence on the scattering angle of the photons with respect to the incident electron/positron. Depending on the possible new physics scenario, a departure of the measured differential cross-section of $e^+e^- \to \gamma\gamma$ from the Standard Model expectations, could then be interpreted as a measure of the energy scale of the QED breakdown [5, 6], of the characteristic energy scales of $e^+e^-\gamma\gamma$ contact interactions [7], of the mass of excited electrons within composite models [8] or of the string mass scale [9, 10] (which could be of the order of the electroweak scale in the framework of models with gravity propagating in large extra-dimensions).

The data recorded by DELPHI at LEP 2 were treated according to common reconstruction procedures, selection criteria and treatment of systematic uncertainties. Previous results concerning the process $e^+e^- \to \gamma\gamma(\gamma)$, using DELPHI LEP 1 data are reported in reference [11]. An analysis of the LEP 2 data collected in 1996 and 1997 can be found in reference [12], while the analysis of the 1998 and 1999 DELPHI data, from which the present analysis framework evolved is reported in [13]. The results reported in the previous publications concerning the analyses of LEP 2 data are superseded by the results hereby reported. The most recently published results from the other LEP collaborations can be found in references [14, 15, 16].

2 Data sample and apparatus

The data analysed were recorded with the DELPHI detector at LEP 2 from 1996 through 2000. They were grouped in ten subsets, as listed in table 1, according to their centre-of-mass energy value or, in the case of the year 2000 data, split in two sets corresponding to different data processings (reconstruction procedures). This was made necessary due to an irreversible failure in a sector of the Time Projection Chamber, one of the most important tracking detectors, during the last part of the data taking period.

Events were generated for all the processes at the different centre-of-mass energies and passed through the full DELPHI simulation and reconstruction chain. The event generator used to simulate the QED process $e^+e^- \to \gamma\gamma(\gamma)$ was that of reference [2] while Bhabha ($e^+e^- \to e^+e^-(\gamma)$) and Compton ($e^\pm\gamma$) scattering[1] backgrounds were simulated with the BHWIDE [17] and TEEG [18] generators and $e^+e^- \to f\bar{f}(\gamma)$ events, including

[1]Compton events are produced when a beam electron is scattered off by a quasi-real photon radiated by the other incoming electron, resulting mostly in final states with one photon and one visible electron, the remaining $e^\pm$ being lost in the beam pipe.

$e^+e^- \to \nu\bar{\nu}\gamma\gamma$ events, were generated with KORALZ [19]. Two photon collision events, yielding $e^+e^-f\bar{f}$ final states, were generated with BDK/BDKRC [20].

The luminosity corresponding to the data sets analysed was measured by counting the number of Bhabha events at small polar angles [21]. These were recorded with the Small angle TIle Calorimeter (STIC) that consisted of two cylindrical electromagnetic calorimeters surrounding the beam pipe at a distance of $\pm$220 cm from the interaction point, covering the polar angle[2] range from 2° to 10° and from 170° to 178°.

Photon detection and reconstruction relied on the trigger and energy measurements provided by the electromagnetic calorimeters: the STIC, the High density Projection Chamber (HPC) in the barrel region and the Forward ElectroMagnetic Calorimeter (FEMC) in the endcaps. The HPC was a gas-sampling calorimeter, composed of 144 modules, each with 9 longitudinal samplings in 41 lead layers and a scintillator layer which provided first and second level trigger signals. It covered polar angles between 42° and 138°. The FEMC was a lead glass calorimeter, covering the polar angle regions $[11°, 35°]$ and $[145°, 169°]$. The barrel DELPHI electromagnetic trigger [22] required coincidences between scintillator signals and energy deposits in the HPC while in the forward region the electromagnetic trigger was given by energy deposits in the FEMC lead-glass counters.

The tracking system allowed the rejection of charged particles and the recovery of photons converting inside the detector. The DELPHI barrel tracking system relied on the Vertex Detector (VD), the Inner Detector (ID), the Time Projection Chamber (TPC) and the Outer Detector (OD). In the endcaps, the tracking system relied also on the VD and the TPC (down to about 20° in polar angle), and on the Forward Chambers A and B (FCA, FCB). The VD played an important role in the detection of charged particle tracks coming from the interaction point.

A more detailed description of the DELPHI detector, of the triggering conditions and of the readout chain can be found in [1, 22].

3 Event selection

Preselection requirements enabled the rejection of most final states not compatible with multi-photon events. Energy deposits in the HPC, FEMC and HCAL were used if their energy was greater than 500 MeV, 400 MeV and 900 MeV respectively. The multiplicity of well reconstructed charged particle tracks was required to be less than 6, where a well reconstructed charged particle track had to have momentum above 200 MeV/c, z and $r\phi$ impact parameters below 4 cm/$\sin\theta$ and 4 cm respectively, $\Delta p/p$ below 1.5 and could not have left signals in the VD only. Events containing signals in the muon chambers were rejected and the visible energy (in the polar angle range between 20°and 160°) was required to be greater than $0.1\sqrt{s}$. After the application of the preselection requirements, the data sample was dominated by Bhabha and Compton scattering events. At $\sqrt{s}$=206 GeV, they amounted respectively to about 81% and 9% of the preselected simulated sample, while the $e^+e^- \to \gamma\gamma(\gamma)$ events constituted about 3%. The remaining 7% corresponded to $e^+e^- \to e^+e^-\gamma\gamma$ ($\sim$4%), $e^+e^- \to \tau^+\tau^-(\gamma)$ ($\sim$1%) and $e^+e^- \to \nu\bar{\nu}\gamma\gamma$ ($\sim$0.7%) events and to residual contributions from other processes. The next steps of the analysis consisted in

[2]The polar angle, θ, was defined with respect to the direction of the electron beam.

first reconstructing photons, then selecting multi-photonic final states and finally selecting $e^+e^- \to \gamma\gamma$ events.

3.1 Photon reconstruction

Photons are characterised by leaving energy in the electromagnetic calorimeters and no signals in the tracking devices, with the exception of photons converting within the tracking system. In both cases, the information provided by the calorimeters can be the input for photon reconstruction algorithms. A clustering algorithm was therefore developed, consisting of a double cone centered on calorimeter energy deposits, in which the inner cone should contain the energy deposited by the photon, while the absence of calorimetric deposits or charged tracks beyond a predefined energy threshold in the outer cone should ensure its isolation from other objects.

The parameters of the double-cone algorithm were optimized for the selection of the signal events using simulated $e^+e^- \to \gamma\gamma(\gamma)$ events. The best performance was obtained by choosing two cones with vertex in the geometric centre of the DELPHI detector and half-opening angles of 10° and 12° respectively. The energy in the inner cone was required to be above 5 GeV, while the total energy collected in the region between the two cones had to be below 5 GeV.

3.2 Selection of multi-photonic events

The main contamination to $e^+e^- \to \gamma\gamma(\gamma)$ events after preselection and photon reconstruction came from radiative Bhabha events with one non-reconstructed electron and the other electron lost in the beam pipe and from Compton scattering ($e^{\pm}\gamma$) events. Both backgrounds were dramatically reduced using the Vertex Detector as a veto against charged particles coming from the interaction point. Other sources of contamination of photonic final states such as calorimeter noise were eliminated by taking into account the profile of photonic showers in the electromagnetic and hadronic calorimeters. The photon identification criteria based on the response of the VD and of the calorimeters are listed below:

- Charged particles coming from the interaction point were rejected by requiring that no VD track element[3] was within 3° in azimuthal angle[4] from photons reconstructed in the barrel. The corresponding angle in the endcaps was 10°.
- In order to be compatible with the energy profile of photons in the HPC, particles reconstructed within the polar angle range $\theta \in [42°, 138°]$ were required to either have energy deposits in at least 3 HPC layers - each containing more than 5% of the electromagnetic energy of the particle - or to have their azimuthal angle coinciding with the HPC modular divisions within ±1°.
- Noise in the FEMC crystals was rejected by requiring that particles reconstructed within the FEMC acceptance had given signals in at most 50 lead-glass blocks and that at least 15% of their electromagnetic energy was in one of the blocks.

[3] A VD track element was defined by the presence of at least two signals in different VD layers separated in azimuthal angle by at most 0.5°.

[4] The azimuthal angle, ϕ, in the plane transverse to the beam direction, was defined with respect to the x-axis pointing to the centre of LEP.

- Photons reaching the hadronic calorimeter should leave all their energy in its first layer, therefore, the reconstructed particles were required to have less than 5 GeV of hadronic energy associated to them or that at least 90% of their hadronic energy component was recorded in the first layer of the HCAL.

The selected sample consisted of events with at least two reconstructed particles fulfilling the photon reconstruction requirements and background rejection criteria described above. The two most energetic photons had to be located in the polar angle range between 25° and 155° and at most one converted photon, i.e. a reconstructed photon associated to well reconstructed charged particle tracks not associated to VD track elements, was allowed per event. The numbers of events thus selected from real and simulated data are compared, as a function of $\sqrt{s}$, in table 2. Figure 1 displays the selected event distributions of the polar angle, of the photon energy (normalised to $\sqrt{s}$) and of the angle between the two most energetic photons for the full data set and compares them to the Standard Model predictions. For all distributions, the solid circles represent real data events, the shaded histogram represents the $e^+e^- \to \gamma\gamma(\gamma)$ prediction and the hatched histogram the remaining background processes: Bhabha and Compton scattering and $e^+e^- \to \nu\bar{\nu}\gamma\gamma(\gamma)$ events. An overall deficit of about 4.5% was observed in the global data set with respect to the simulation predictions. It is attributed to the photon trigger efficiency, which is lower in the barrel region of the detector, and to differences between the real detector and its simulated description, especially in aspects of the calorimeter performances. Both effects are discussed and accounted for in section 4.

3.3 Selection of $e^+e^- \to \gamma\gamma$ events

Events were considered as possibly due to the $e^+e^- \to \gamma\gamma$ process if they contained two photons and no other reconstructed particles. Moreover, the two photons had to:

- have an energy greater than $0.15\sqrt{s}$ each;
- be separated by a spatial angle of at least 130°;
- be contained within the polar angle acceptance of the VD and of the electromagnetic calorimeters:
  $\theta \in [25°, 35°] \cup [42°, 88°] \cup [92°, 138°] \cup [145°, 155°]$.

The $e^+e^- \to \gamma\gamma$ selection resulted in a very low rate of expected background events. The contamination from Bhabha events was already small after the selection criteria for multi-photon events were imposed (see table 2), while the contribution from Compton scattering and $\nu\bar{\nu}\gamma\gamma$ events was drastically reduced mainly by the requirement that the spatial angle between both photons was large, but also by the energy cut. The total contamination in the $e^+e^- \to \gamma\gamma$ samples was found to be less than 0.2%. Since this contamination corresponded to a very small number of background simulated events, it was fully taken into account as a systematic uncertainty in the determination of the cross-section for $e^+e^- \to \gamma\gamma$. The final numbers of selected and expected events are given in table 3.

4 Determination of the Born level cross-section for the process $e^+e^- \to \gamma\gamma(\gamma)$

The analysis of the process $e^+e^- \to \gamma\gamma$ was based on the study of distributions of $|\cos\theta^*|$ for the selected samples, where θ^* is the polar angle of the photons with respect to the direction of the incident electron in the centre-of-mass of the e^+e^- collision. $|\cos\theta^*|$ is defined by:

$$|\cos\theta^*| = \sin[0.5(\theta_{\gamma 1} - \theta_{\gamma 2})] / \sin[0.5(\theta_{\gamma 1} + \theta_{\gamma 2})] \quad (1)$$

where $\theta_{\gamma 1}$ and $\theta_{\gamma 2}$ are the polar angles of the photons in the laboratory frame. This parameterisation of the polar angle of the photons enables the measurement of the differential cross-section of $e^+e^- \to \gamma\gamma$ to be insensitive to Initial State Radiation photons radiated collinearly to the beam.

In the present analysis, the retained $|\cos\theta^*|$ acceptance was divided into 16 intervals: the barrel part of the detector, corresponding to $[0.035, 0.731]$ with 14 bins (each covering $|\Delta\cos\theta^*| = 0.0505$, except for the last two, for which $|\Delta\cos\theta^*| = 0.045$) and the forward region, corresponding to $[0.819, 0.906]$, which was divided in two equal bins.

4.1 Evaluation of the selection efficiency

The efficiency for selecting the $\gamma\gamma$ samples was evaluated as a function of $|\cos\theta^*|$ using simulated sets of $e^+e^- \to \gamma\gamma(\gamma)$ events generated at different centre-of-mass energies. The average selection efficiency in the barrel region of DELPHI was close to 80%, whereas in the endcaps it was found to be about 52% for data taken prior to 1999 and ∼62% for the remaining data, resulting from improvements in the particle reconstruction algorithms used for the forward region of DELPHI.

Small differences between the real detector response and the detector simulation were observed. These differences came from aspects of the performance of the calorimeters, and were essentially caused by the limited accuracy of the simulation description in the edges of HPC modules. Differences due to the description of the amount of material in front of the calorimeters could also arise, especially in the endcaps. In order to investigate these differences, sets of real and simulated Bhabha events were selected using the information provided by the tracking devices alone. The two photon selection criteria based on calorimeter information were then imposed on the selected samples. The differences between the effect of the selection criteria on real and simulated data were then parameterised as a correction factor $\mathcal{R}$, which was taken as the ratio between simulated and real data rates of Bhabha events fulfilling all criteria. The correction factor $\mathcal{R}$ reflects the necessary correction to the selection efficiency as evaluated from the simulation of $e^+e^- \to \gamma\gamma(\gamma)$.

The corrections to the selection efficiency were evaluated as a function of the $|\cos\theta^*|$ interval and of $\sqrt{s}$. Their average value for each analysed data set was found to be above 1.0 by 1% to about 2.8%, depending on the data set, reflecting an over-estimation of the selection efficiency. The main contribution for this difference was found to come from the barrel region of DELPHI, with exception for the 206.3 GeV data set where the correction to the selection efficiency in the endcaps amounted to 4.7%. The average

selection efficiencies, for the barrel and endcaps of DELPHI, including the corresponding corrections are displayed in table 3 as a function of $\sqrt{s}$.

4.2 Evaluation of the trigger efficiency

The trigger efficiency for $\gamma\gamma$ final states without photon conversions was computed with Bhabha ($e^+e^- \to e^+e^-$) events and using the redundancy of the electromagnetic trigger with the track trigger. It was evaluated as a function of $|\cos\theta^*|$ for each data set and taking into account the different trigger settings.

The $\gamma\gamma$ trigger efficiency values in the forward region were close to 100% for all data sets. As for the barrel region, average values close to 97% were obtained. The lower value obtained for the 172 GeV data set (78%) was due to a malfunctioning of the barrel single photon trigger, present during part of the 1997 data taking period. The average trigger efficiencies for the barrel and endcaps are displayed in table 3.

Final states with one converted photon, were triggered by the single track coincidence trigger, whose efficiency was nearly 100% [22].

4.3 Radiative corrections

The event selection does not correspond to the Born level contribution from $e^+e^- \to \gamma\gamma$ since no selection criteria can remove the higher order contributions coming from soft *bremsstrahlung* and the exchange of virtual gauge bosons. In order to take such higher order corrections into account, the radiative effects were estimated using the $e^+e^- \to \gamma\gamma(\gamma)$ physics generator of Berends and Kleiss [2] which computes the cross-section for $e^+e^- \to \gamma\gamma$ up to $\mathcal{O}(\alpha^3)$. The radiative correction factor R_i was evaluated as a function of $|\cos\theta^*|$ by generating 10^7 events at the average centre-of-mass energy value corresponding to each data set, although its variation within the considered $\sqrt{s}$ range was negligible. It was taken as the ratio between the $e^+e^- \to \gamma\gamma(\gamma)$ cross-section computed up to order α^3 to the Born level cross-section ($\mathcal{O}(\alpha^2)$), which for a given $\Delta\cos\theta^*$ acceptance (including the θ^* complement with respect to 90°) is given by:

$$\sigma^0_{QED}(\Delta\cos\theta^*) = \frac{2\pi\alpha^2}{s}\left[\ln\frac{1+\cos\theta^*}{1-\cos\theta^*} - \cos\theta^*\right]_{\Delta\cos\theta^*} \tag{2}$$

The radiative correction factor ranged between 1.03 for events with high $|\cos\theta^*|$ values (forward events) and about 1.07 for low values of $|\cos\theta^*|$, and are displayed as a function of $|\cos\theta^*|$ in table 4.

4.4 Systematic uncertainties

The systematic uncertainty on the cross-section measurement was obtained for each $|\cos\theta^*|$ interval and for the ten data subsets by adding in quadrature the respective relative residual background expectations, the uncertainties on the selection efficiency and on the corresponding correction, the uncertainty on the trigger determination, the statistical error on the radiative corrections determination and the uncertainty from the determination of the luminosity.

The uncertainty on the determination of the selection efficiency had three components, coming from the statistical uncertainty due to the finite Monte Carlo statistics, from the uncertainty on its correction and from the experimental resolutions of the variables used in the $e^+e^- \to \gamma\gamma$ selection. The latter were, as described in sections 3.3 and 4, the angle between the two photons, their energy and $|\cos\theta^*|$. The uncertainties were evaluated, for each of the $e^+e^- \to \gamma\gamma(\gamma)$ simulated samples, from the distributions of the difference between the values of the corresponding variables at generator level and after being passed through the full detector simulation and reconstruction chain. The uncertainties on the energy of the photons were taken as the r.m.s. values of Gaussian fits to these difference distributions. The same procedure was followed for the uncertainty on $\cos\theta^*$ which was evaluated independently for each $|\cos\theta^*|$ interval. The uncertainty on the spatial angle between the photons was taken as the quadratic sum of the shift in the central value and of half of the full width at half maximum of the distributions.

The uncertainty in the luminosity determination had both experimental and theoretical contributions. The experimental contribution corresponds to a $\pm 0.5\%$ systematic uncertainty in the measurement of the luminosity. The theoretical contribution to the luminosity determination uncertainty was taken to be $\pm 0.25\%$, from the Bhabha event generator BHLUMI [23]. A total error of $\pm 0.56\%$ on the luminosity determination was therefore obtained by adding in quadrature both the experimental and theoretical uncertainties.

The overall values for the systematic uncertainty associated to each data sample are presented in table 5, as well as the specific contributions coming from different sources of systematic error. The dominant contribution to the systematic error came from the uncertainty on the determination of the selection efficiency.

4.5 Cross-section for $e^+e^- \to \gamma\gamma$

The differential cross-section for $e^+e^- \to \gamma\gamma$ was computed for each $|\cos\theta^*|$ interval (i) as:

$$\frac{d\sigma_i^0}{d\Omega} = \frac{1}{2\pi(\Delta\cos\theta^*)_i}\frac{1}{\mathcal{L}}\frac{N_i^{\gamma\gamma}}{\varepsilon_i R_i} \tag{3}$$

where $\mathcal{L}$ is the integrated luminosity of the considered data set, $N_i^{\gamma\gamma}$ is the corresponding number of selected events, ε_i is the corresponding product of trigger efficiency and selection efficiencies (including corrections) and R_i is the radiative correction factor. The numbers of events selected from each data sample, are compared to the simulation predictions (accounting for trigger efficiency and for selection efficiency corrections) in table 3. A total number of 2679 events were selected from data while 2761 ± 15 were expected from the $e^+e^- \to \gamma\gamma(\gamma)$ simulation, taking into account the trigger efficiency and the selection efficiency corrections. In table 6, the number of events and efficiency (the product of trigger and selection efficiencies) are displayed for each data set as a function of $|\cos\theta^*|$.

For the purpose of combining the DELPHI data with the data taken by the other LEP experiments, a different $|\cos\theta^*|$ binning is used in table 7 to display the numbers of events and the analysis efficiency for a subsample of 2206 events, among the the 2679 events selected. The corresponding radiative correction factors are displayed as a function of $|\cos\theta^*|$ in table 4.

The Born level differential cross-section distributions for the ten data sets are compared in figure 2 to the corresponding theory predictions. An average centre-of-mass energy of 195.6 GeV was calculated for the entire data sample by weighting the integrated luminosities of the ten data sets by the corresponding $1/s$ factor, in order to take into account the dependence of the Born level cross-section on the centre-of-mass energy (equation 2). The average differential cross-section is compared to the theoretical prediction in figure 3 (top) and in table 8. It was computed for each $|\cos\theta^*|$ interval from expression 3, where $\mathcal{L}$ was the integrated luminosity of the full data set and the third fraction was replaced by the sum of the number of events in each bin divided by the corresponding correction, consisting of the product of the efficiency and of the radiative correction factor.

The total visible cross-section for the process $e^+e^- \to \gamma\gamma$, integrated over the full $|\cos\theta^*|$ acceptance, i.e. $|\cos\theta^*| \in [0035, 0.731] \cup [0.819, 0.906]$, was evaluated for each centre-of-mass energy, using the expression:

$$\sigma^0_{dat} = \frac{1}{\mathcal{L}} \sum_{i=1}^{Nbins} \frac{N_i^{\gamma\gamma}}{\varepsilon_i R_i} \tag{4}$$

The visible cross-section measurements as a function of $\sqrt{s}$ are compared to theory in figure 3 (bottom) and their values (with statistical and systematic uncertainties) are displayed in table 9. The $\chi^2/ndof$ of the measured differential cross-section distributions with respect to theory[5] were computed for each data set and are also presented in table 9, showing the agreement between the measurement and theory. The total visible cross-section at the average centre-of-mass energy of 195.6 GeV was computed as the ratio between the sum of the number of events found in each bin and for all data sets, corrected by the corresponding $1/(\varepsilon_i R_i)$ factors, and the integrated luminosity of the full data sample. The obtained cross-section was $5.66 \pm 0.11 \pm 0.03$ pb, in agreement with the 5.83 pb expectation from the Standard Model.

The Born level cross-section measurements in the region $0.035 < |\cos\theta^*| < 0.731$, were corrected to the full barrel acceptance of DELPHI, $0.000 < |\cos\theta^*| < 0.742$, and the obtained values are displayed in figure 4 as a function of the centre-of-mass energy, along with previously published results, derived from LEP 1 data collected between 1990 and 1992 [11] and from LEP 1.5 data collected at $\sqrt{s}$=130-136 GeV [12].

5 Deviations from QED

Possible deviations from QED are described in the context of several different models in which the Born level differential cross-section for $e^+e^- \to \gamma\gamma$ is expressed, as in (5), as the sum of the QED term and of a deviation term, the latter parameterised as a function of an energy (or mass) scale of relevance for the model tested.

$$\frac{d\sigma_i^0}{d\Omega} = \frac{\alpha^2}{s}\left(\frac{1+\cos^2\theta^*}{1-\cos^2\theta^*}\right) + \left(\frac{d\sigma}{d\Omega}\right)^D \tag{5}$$

[5]The theoretical uncertainty on the QED prediction, estimated to be below ±1%, was neglected.

The 95% C.L. lower limits on the free parameters – energy/ mass scales – for different models were extracted using binned maximum likelihood functions. These were built as the joint probabilities for the number of observed events in each $|\cos\theta^*|$ bin and data set, given the number of expected events from theory. For each model, the number of expected events was a function of the corresponding parameter, written in the form of an estimator ξ, which, whenever possible, was chosen to yield an approximately Gaussian distribution for the likelihood function. The systematic uncertainties were taken into account as the r.m.s. values of Gaussian probability density functions of free normalization parameters. The maximization of the likelihood functions was performed using the program MINUIT [24]. For each model, the results were translated in terms of central $\bar{\xi}$ and positive and negative r.m.s. values $\sigma_\pm$ for the estimators, whereas the 95% C.L. lower limits for the parameters were obtained by renormalising the joint probability distribution to their physically allowed region [25].

The different models and the 95% C.L. lower bounds derived for the corresponding parameters presented in detail in the following sections are summarised in table 10.

5.1 QED cutoff

The most general way to parameterise a deviation from QED is by the introduction of a QED cutoff, representing the energy scale of the QED breakdown, Λ, [5, 6]. This is the scale up to which the $e\gamma$ interaction can be described as point-like. The deviation cross-section would be given by expression (6) (where α is the fine-structure constant) which allows for negative and positive interference in the form of the $\pm 1/\Lambda_\pm^4$ parameterisation.

$$\left(\frac{d\sigma}{d\Omega}\right)^D = \pm\frac{\alpha^2 s}{2}(1+\cos^2\theta^*)\frac{1}{{\Lambda_\pm}^4} \tag{6}$$

The result of the maximum likelihood fit to data yielded -59^{+40}_{-39} TeV^{-4} for the estimator $1/\Lambda_\pm^4$, resulting in lower bounds for the energy scale of the QED breakdown of 379 GeV and 300 GeV for Λ_+ and Λ_-, respectively.

5.2 Search for contact interactions

Bounds on the mass scale of the $e^+e^-\gamma\gamma$ contact interaction can be parameterised in different ways, depending on the dimensionality of the effective Lagrangian describing the interaction [7]. Operators of dimension 6, 7 and 8 translate into the characteristic scales Λ_6, Λ_7 and Λ_8. The corresponding deviation cross-sections can be expressed as:

$$\left(\frac{d\sigma}{d\Omega}\right)^D = \alpha s(1+\cos^2\theta^*)\frac{1}{{\Lambda_6}^4} \quad , \tag{7}$$

$$\left(\frac{d\sigma}{d\Omega}\right)^D = \frac{s^2}{32\pi}\frac{1}{{\Lambda_7}^6} \quad , \tag{8}$$

$$\left(\frac{d\sigma}{d\Omega}\right)^D = \frac{s^2 M_e^2}{64\pi}\frac{1}{{\Lambda_8}^8} \quad , \tag{9}$$

where M_e is the electron mass.

Maximum likelihood fits to data yielded the results $1/\Lambda_6^4 = -0.22^{+0.15}_{-0.14}$ TeV^{-4}, $1/\Lambda_7^6 = -4.1^{+3.2}_{-3.1}$ TeV^{-6} and $1/\Lambda_8^8 = (-31 \pm 24) \times 10^{12}$ TeV^{-8}, resulting in 95% C.L. lower bounds on the characteristic energy scales for contact interactions, Λ_6, Λ_7 and Λ_8 of 1.5 TeV, 790 GeV and 21 GeV respectively.

5.3 Search for excited electrons

Within the framework of composite models, deviations from QED could also follow from the t-channel exchange of an excited electron. In the case of an $e^*e\gamma$ chiral magnetic coupling [8], the deviation from the QED differential cross-section is expressed by:

$$\left(\frac{d\sigma}{d\Omega}\right)^D = \frac{\alpha^2}{4}\left(\frac{f_\gamma}{\Lambda}\right)^2 \sum_{n=1}^{2}\left[\frac{(1+i^{2n}\cos\theta^*)^2}{Y+i^{2n}\cos\theta^*}\left(1+\frac{s}{4}\left(\frac{f_\gamma}{\Lambda}\right)^2\frac{1-\cos^2\theta^*}{Y+i^{2n}\cos\theta^*}\right)\right] \tag{10}$$

where i is the imaginary number and Y=1+2$M_{e^*}^2/s$, M_{e^*} being the mass of the excited electron. f_γ/Λ is the coupling constant with $f_\gamma = -\frac{1}{2}(f+f')$, where f and f' are weight factors associated to the different gauge groups.

In order to derive a lower bound on the excited electron mass, f_γ/Λ was set to $1/M_{e^*}$ in expression (10). A 95% C.L. lower bound $M_{e^*} = 295$ GeV/c^2 was derived, corresponding to $1/M_{e^*}^4 = -142^{+104}_{-113}$ (TeV/c^2)$^{-4}$. In addition, limits on the coupling constant f_γ/Λ as a function of M_{e^*} were derived by performing a scan over M_{e^*} and are presented in figure 5.

The framework adopted in the interpretation of the previous DELPHI results [12, 13], corresponding to a purely magnetic $e^*e\gamma$ coupling [26], is strongly limited by $g_e - 2$ measurements [27, 28] for the energy scales accessible at LEP. In such a framework, the maximum likelihood fit yielded $1/M_{e^*} = -69^{+49}_{-53}$ (TeV/c^2)$^{-4}$ and the 95% C.L. lower bound on M_{e^*} was 356 GeV/c^2 (for λ_γ=1, where $f_\gamma/\Lambda = \sqrt{2}\lambda_\gamma/M_{e^*}$).

5.4 Search for TeV-scale quantum gravity

The phenomenological implications of large extra-dimensions [9, 10] have lead to the suggestion of the possibility of observing the effect of virtual graviton exchange at LEP as a departure of the differential cross-section for $e^+e^- \to \gamma\gamma$ from the QED prediction. The deviation cross-section, given by expression (11), can be parameterised as a function of the string mass scale M_s, which in some string models could be as low as the electroweak scale, and of a phase factor, λ, conventionally taken to be ± 1 [6].

$$\left(\frac{d\sigma}{d\Omega}\right)^D = -\frac{\alpha s}{2\pi}(1+\cos^2\theta^*)\frac{\lambda}{M_s^4} \tag{11}$$

A maximum likelihood fit yielded $\pm 1/M_s^4 = 1.36^{+0.92}_{-0.90}$ (TeV/c^2)$^{-4}$, resulting in lower limits on the string mass scale of 771 GeV/c^2 and 985 GeV/c^2 for $\lambda = 1$ and $\lambda = -1$, respectively.

[6] The ratio λ/M_s^4 which follows the notation of [29] is related to the quantum gravity scale Λ_T in Ref. [9] as: $\frac{|\lambda|}{M_s^4} = -\pi/2(1/\Lambda_T^4)$.

6 Summary

The reaction $e^+e^- \to \gamma\gamma(\gamma)$ was studied using the LEP 2 data collected with the DELPHI detector at centre-of-mass energies ranging from 161 GeV to 208 GeV, corresponding to a total integrated luminosity of 656.4 pb^{-1}. The differential and total cross-sections for the process $e^+e^- \to \gamma\gamma$ were measured. Good agreement between the data and the QED prediction was found. The absence of a deviation from QED was used to set 95% C.L. lower limits on the parameters of models predicting deviations from QED. The QED cut-off parameters Λ_+ and Λ_- were found to be greater than 379 GeV and 300 GeV, respectively. Lower limits on the characteristic energy scales of $e^+e^-\gamma\gamma$ contact interactions, $\Lambda_6 = 1.5$ TeV, $\Lambda_7 = 790$ GeV and $\Lambda_8 = 21$ GeV were obtained. A lower limit for the mass of an excited electron with a chiral magnetic coupling to photon-electron pairs, $M_{e^*} > 295$ GeV/c^2, was obtained. The possible contribution of virtual gravitons to the process $e^+e^- \to \gamma\gamma$ was probed, resulting in the bounds $M_s > 771$ GeV/c^2 and $M_s > 985$ GeV/c^2 for $\lambda = 1$ and $\lambda = -1$ respectively (where λ is a phase factor in some quantum gravity models).

References

[1] DELPHI Coll., P. Aarnio et al., *Nucl. Instr. and Meth.* **A303** (1991) 233;
DELPHI Coll., P. Abreu et al., *Nucl. Instr. and Meth.* **A378** (1996) 57.

[2] F.A. Berends and R. Kleiss, *Nucl. Phys.* **B186** (1981) 22.

[3] M. Böhm and T. Sack, *Zeit. Phys.* **C33** (1986) 157.

[4] J. Fujimoto, M. Igarashi and Y. Shimizu, *Prog. of Theor. Phys.* **Vol. 77** (1987) 118.

[5] S. Drell, *Annals Phys.* **4** (1958) 75.

[6] F.E. Low, *Phys. Rev. Lett.* **14** (1965) 238.

[7] O.J.P. Éboli, A.A. Natale and S.F. Novaes, *Phys. Lett.* **B271** (1991) 274.

[8] B. Vachon, *"Excited electron contribution to the $e^+e^- \to \gamma\gamma$ cross-section"*, hep-ph/0103132 v2 (28 April 2004).

[9] G.F. Giudice, R. Rattazzi and J.D. Wells, *Nucl. Phys.* **B544** (1999) 3; revised version in hep-ph/9811291 (13 March 2000).

[10] K. Agashe and N.G. Deshpande, *Phys. Lett.* **B456** (1999) 60.

[11] DELPHI Coll., P. Abreu et al., *Phys. Lett.* **B327** (1994) 386.

[12] DELPHI Coll., P. Abreu et al., *Phys. Lett.* **B433** (1998) 429.

[13] DELPHI Coll., P. Abreu et al., *Phys. Lett.* **B491** (2000) 67.

[14] ALEPH Coll., A. Heister et al., *Eur. Phys. J.* **C28** (2003) 1.

[15] L3 Coll., P. Achard et al., *Phys. Lett.* **B531** (2002) 28.

[16] OPAL Coll., G. Abbiendi et al., *Eur. Phys. J.* **C26** (2003) 331.

[17] S. Jadach, W. Placzek and B.F.L. Ward, *Phys. Lett.* **B390** (1997) 298.

[18] D. Karlen, *Nucl. Phys.* **B289** (1987) 23.

[19] S. Jadach, B.F.L. Ward and Z. Was, *Comp. Phys. Comm.* **79** (1994) 503;
S. Jadach, B.F.L. Ward and Z. Was, *Comp. Phys. Comm.* **124** (2000) 233.

[20] F.A.Berends,P.H.Daverveldt and R.Kleiss, *Comp. Phys. Comm.* **40** (1986) 285;
F.A.Berends,P.H.Daverveldt and R.Kleiss, *Comp. Phys. Comm.* **40** (1986) 271.

[21] S.J. Alvsvaag et al., *Nucl. Instr. and Meth.* **A425** (1999) 106.

[22] DELPHI Trigger Group, A. Augustinus et al., *Nucl. Instr. and Meth.* **A515** (2003) 782.

[23] S. Jadach, O. Nicrosini et al., *"Event Generators for Bhabha Scattering"* CERN Yellow Report 96-01, vol 2, p.299.

[24] F. James, *"MINUIT, Function Minimization and Error Analysis, V94.1"* CERN Program Library Long Writeup D506, CERN (1994).

[25] Particle Data Group, C. Caso et al., *Eur. Phys. J.* **C3** (1998) 1.

[26] A. Blondel et al., CERN-EP-87-50, appeared in Proceedings of ECFA Workshop on LEP 200, CERN 87-08 (ECFA87-108), p.414.

[27] F.M. Renard, *Phys. Lett.* **B116** (1982) 264.

[28] S.J. Brodsky and S.D. Drell, *Phys. Rev.* **D22** (1980) 2236.

[29] J.L. Hewett, *Phys. Rev. Lett.* **82** (1999) 4765.

Year	1996		1997	1998	1999				2000	
$\sqrt{s}$ (GeV)	161.3	172.0	182.7	188.6	191.6	195.5	199.5	201.6	205.7	206.3
$\mathcal{L}$ (pb^{-1})	8.4	8.8	49.0	152.6	25.1	75.9	82.5	40.0	160.3	54.0

Table 1: Data sets used in the analysis, corresponding average centre-of-mass energies and integrated luminosities. The data taken during the year 2000 were split in two data sets, before and after an irreversible failure in a sector of the TPC.

$\sqrt{s}$ (GeV)	N_{QED}	$N_{Compton}$	N_{Bhabha}	$N_{\nu\bar{\nu}\gamma\gamma}$	N_{SM}^{total}	N_{data}
161.3	69.34± 1.99	0.99±0.91	0.04±0.02	0.43±0.04	70.8± 2.2	76
172.0	64.23± 1.85	0.91±0.84	0.03±0.02	0.46±0.04	65.6± 2.0	47
182.7	316.97± 9.11	3.57±2.03	0.06±0.02	2.54±0.23	323.1± 9.3	304
188.6	892.97± 4.81	7.99±0.50	0.07±0.05	7.91±0.73	908.9± 4.9	888
191.6	147.87± 1.27	1.37±0.25	0.07±0.01	1.55±0.17	150.9± 1.3	133
195.5	429.80± 3.68	3.99±0.74	0.19±0.03	4.00±0.35	438.0± 3.9	437
199.5	453.86± 3.91	4.16±0.77	0.20±0.03	4.39±0.33	462.6± 4.0	434
201.6	215.45± 1.86	1.97±0.37	0.10±0.02	1.73±0.20	219.3± 1.9	207
205.7	835.04± 7.20	10.65±1.54	0.38±0.03	8.13±0.76	854.2± 7.4	804
206.3	275.72± 3.16	3.55±0.75	0.12±0.03	2.47±0.28	281.9± 3.3	274
total	3701.29±14.48	39.15±3.19	1.23±0.09	33.61±1.24	3775.3±14.9	3604

Table 2: Number of events remaining in all real and simulated data samples after the application of the multi-photonic event selection criteria and before corrections for trigger and selection efficiency.

$\sqrt{s}$ (GeV)	$<\varepsilon_{sel}^{\gamma\gamma}>$		$<\varepsilon_{trig}^{\gamma\gamma}>$		$N^{\gamma\gamma}$	
	Barrel	Endcaps	Barrel	Endcaps	QED	data
161.3	0.770±0.020	0.519±0.026	0.97±0.01	$1.000^{+0.000}_{-0.003}$	51.5± 2.8	57
172.0	0.766±0.020	0.518±0.026	0.78±0.03	$1.000^{+0.000}_{-0.003}$	41.0± 2.5	33
182.7	0.773±0.015	0.522±0.025	0.977±0.005	0.998±0.001	234.1± 8.0	220
188.6	0.766±0.007	0.536±0.011	0.984±0.002	0.9998±0.0002	666.5± 6.8	673
191.6	0.791±0.007	0.615±0.014	0.979±0.007	$1.000^{+0.000}_{-0.001}$	114.6± 1.9	102
195.5	0.777±0.006	0.618±0.013	0.976±0.004	$1.0000^{+0.0000}_{-0.0003}$	327.3± 3.8	341
199.5	0.772±0.007	0.609±0.013	0.963±0.005	0.9993±0.0005	336.6± 4.1	325
201.6	0.783±0.008	0.622±0.013	0.983±0.005	$1.0000^{+0.0000}_{-0.0007}$	162.5± 2.6	150
205.7	0.775±0.006	0.608±0.013	0.976±0.003	0.9989±0.0004	620.7± 7.0	575
206.3	0.781±0.012	0.589±0.015	0.964±0.006	0.9989±0.0008	206.4± 3.9	203
total					2761.2±15.2	2679

Table 3: Average selection efficiency (with full uncertainties), and average trigger efficiency for $\gamma\gamma$ (with statistical uncertainties) in the barrel and endcaps of DELPHI, number of events expected from simulation, including selection and trigger efficiency corrections and total number of $e^+e^- \to \gamma\gamma$ events selected from each of the ten data samples.

$\lvert\cos\theta^*\rvert$	R	$\lvert\cos\theta^*\rvert$	R
0.0350-0.0855	1.071 ± 0.008		
0.0855-0.1360	1.066 ± 0.008	0.05-0.10	1.070 ± 0.008
0.1360-0.1865	1.065 ± 0.008	0.10-0.15	1.066 ± 0.008
0.1865-0.2370	1.070 ± 0.008	0.15-0.20	1.066 ± 0.008
0.2370-0.2875	1.068 ± 0.007	0.20-0.25	1.070 ± 0.008
0.2875-0.3380	1.056 ± 0.007	0.25-0.30	1.065 ± 0.008
0.3380-0.3885	1.057 ± 0.007	0.30-0.35	1.057 ± 0.007
0.3885-0.4390	1.048 ± 0.007	0.35-0.40	1.055 ± 0.007
0.4390-0.4895	1.054 ± 0.006	0.40-0.45	1.050 ± 0.007
0.4895-0.5400	1.059 ± 0.006	0.45-0-50	1.055 ± 0.006
0.5400-0.5905	1.042 ± 0.006	0.50-0.55	1.056 ± 0.006
0.5905-0.6410	1.050 ± 0.005	0.55-0.60	1.044 ± 0.007
0.6410-0.6860	1.031 ± 0.005	0.60-0.65	1.047 ± 0.005
0.6860-0.7310	1.049 ± 0.005	0.65-0.70	1.036 ± 0.005
0.8190-0.8625	1.037 ± 0.004		
0.8625-0.9060	1.035 ± 0.003	0.85-0.90	1.035 ± 0.003

Table 4: $\mathcal{O}(\alpha^3)$ radiative correction factors, R, evaluated from the generator of Berends and Kleiss [2] as a function of $\lvert\cos\theta^*\rvert$ for the binning used in the present analysis and for the binning chosen in order to combine the data of the four LEP collaborations. The dependence of the radiative correction factor with $\sqrt{s}$ is negligible.

$\sqrt{s}$	Systematic uncertainties (%)						
(GeV)	Bkg	ϵ_{sel}	$\mathcal{R}$	ϵ_{trig}	R	$\mathcal{L}$	Total
161.3	0.10	1.94	1.20	0.60	0.13	0.56	2.43
172.0	0.10	1.94	1.24	1.80	0.13	0.56	2.98
182.7	0.06	1.94	0.49	0.23	0.13	1.03	2.27
188.6	0.08	0.72	0.48	0.11	0.13	0.56	1.05
191.6	0.15	0.84	0.55	0.30	0.13	0.56	1.20
195.5	0.14	0.84	0.35	0.18	0.13	0.56	1.10
199.5	0.11	0.82	0.41	0.24	0.13	0.56	1.11
201.6	0.11	0.82	0.51	0.22	0.13	0.56	1.15
205.7	0.09	0.83	0.32	0.14	0.13	0.56	1.07
206.3	0.20	0.95	0.71	0.31	0.13	0.56	1.37

Table 5: Systematic uncertainties on the cross-section measurements computed for the analysed data sets. A data taking instability led to the assignment of a ±1% experimental error to the 182.7 GeV data luminosity (the theoretical error is of ±0.25%).

$\lvert\cos\theta^*\rvert$	$N^{\gamma\gamma}_{data}/\varepsilon^{\gamma\gamma}$				
	161.3 GeV	172.0 GeV	182.7 GeV	188.6 GeV	191.6 GeV
0.0350-0.0855	3/ 0.751	1/ 0.751	5/ 0.653	18/ 0.759	3/ 0.832
0.0855-0.1360	0/ 0.816	1/ 0.816	6/ 0.641	33/ 0.707	3/ 0.802
0.1360-0.1865	2/ 0.973	2/ 0.730	13/ 0.895	28/ 0.761	3/ 0.776
0.1865-0.2370	2/ 0.840	2/ 0.420	11/ 0.708	28/ 0.744	2/ 0.776
0.2370-0.2875	3/ 0.912	0/ 0.608	10/ 0.839	30/ 0.734	4/ 0.847
0.2875-0.3380	2/ 0.833	3/ 0.570	6/ 0.830	33/ 0.696	4/ 0.820
0.3380-0.3885	3/ 0.584	0/ 0.497	5/ 0.761	26/ 0.658	4/ 0.837
0.3885-0.4390	0/ 0.524	0/ 0.458	4/ 0.617	29/ 0.705	2/ 0.800
0.4390-0.4895	5/ 0.735	0/ 0.680	11/ 0.752	32/ 0.772	6/ 0.748
0.4895-0.5400	3/ 0.895	4/ 0.716	11/ 0.836	39/ 0.814	5/ 0.784
0.5400-0.5905	2/ 0.647	3/ 0.543	14/ 0.733	42/ 0.802	6/ 0.808
0.5905-0.6410	5/ 0.669	2/ 0.606	19/ 0.719	38/ 0.776	10/ 0.798
0.6410-0.6860	2/ 0.832	2/ 0.667	21/ 0.769	55/ 0.739	9/ 0.734
0.6860-0.7310	5/ 0.740	3/ 0.514	23/ 0.750	57/ 0.738	1/ 0.698
0.8190-0.8625	5/ 0.581	6/ 0.592	24/ 0.579	80/ 0.596	18/ 0.629
0.8625-0.9060	15/ 0.472	4/ 0.456	37/ 0.478	105/ 0.495	22/ 0.603

$\lvert\cos\theta^*\rvert$	$N^{\gamma\gamma}_{data}/\varepsilon^{\gamma\gamma}$				
	195.5 GeV	199.5 GeV	201.6 GeV	205.7 GeV	206.3 GeV
0.0350-0.0855	9/ 0.762	11/ 0.745	6/ 0.754	20/0.695	6/ 0.760
0.0855-0.1360	10/ 0.742	8/ 0.711	7/ 0.726	17/0.803	6/ 0.777
0.1360-0.1865	21/ 0.740	9/ 0.802	4/ 0.736	23/0.703	6/ 0.889
0.1865-0.2370	10/ 0.821	12/ 0.831	2/ 0.853	30/0.806	9/ 0.838
0.2370-0.2875	7/ 0.768	16/ 0.744	9/ 0.823	17/0.778	8/ 0.930
0.2875-0.3380	6/ 0.738	11/ 0.744	7/ 0.730	19/0.781	10/ 0.854
0.3380-0.3885	12/ 0.762	18/ 0.736	5/ 0.813	29/0.698	10/ 0.523
0.3885-0.4390	15/ 0.726	16/ 0.638	7/ 0.608	24/0.762	11/ 0.619
0.4390-0.4895	15/ 0.821	19/ 0.803	9/ 0.804	17/0.797	8/ 0.886
0.4895-0.5400	29/ 0.782	21/ 0.745	6/ 0.754	32/0.763	9/ 0.762
0.5400-0.5905	19/ 0.810	25/ 0.779	12/ 0.797	36/0.798	9/ 0.818
0.5905-0.6410	28/ 0.789	25/ 0.729	11/ 0.774	34/0.718	16/ 0.762
0.6410-0.6860	25/ 0.709	10/ 0.736	9/ 0.736	52/0.746	12/ 0.732
0.6860-0.7310	28/ 0.716	24/ 0.743	14/ 0.764	51/0.754	21/ 0.712
0.8190-0.8625	44/ 0.642	37/ 0.637	19/ 0.653	76/0.644	33/ 0.630
0.8625-0.9060	63/ 0.601	63/ 0.598	23/ 0.600	98/0.583	29/ 0.560

Table 6: Number of selected data events and efficiencies (selection times trigger efficiencies corrected for the residual discrepancies between real data and simulation) as a function of $|\cos\theta^*|$ and $\sqrt{s}$ within the polar angle range covered by DELPHI's electromagnetic calorimeters: $|\cos\theta^*| \in [0.035, 0.731] \cup [0.819, 0.906]$.

$\lvert\cos\theta^*\rvert$	$N^{\gamma\gamma}_{data}/\varepsilon^{\gamma\gamma}$				
	161.3 GeV	172.0 GeV	182.7 GeV	188.6 GeV	191.6 GeV
0.05-0.10	2/0.876	1/0.876	4/0.775	19/0.773	4/0.834
0.10-0.15	0/0.670	1/0.595	7/0.526	38/0.714	2/0.803
0.15-0.20	2/1.000	3/0.711	13/0.964	23/0.764	4/0.773
0.20-0.25	3/0.790	1/0.429	10/0.672	29/0.731	3/0.799
0.25-0.30	2/0.878	3/0.624	9/0.828	28/0.730	5/0.819
0.30-0.35	2/0.792	0/0.549	8/0.807	32/0.707	2/0.844
0.35-0.40	3/0.595	0/0.481	2/0.732	24/0.661	4/0.840
0.40-0.45	0/0.553	0/0.496	5/0.656	29/0.705	3/0.772
0.45-0-50	6/0.743	1/0.705	12/0.758	41/0.773	5/0.763
0.50-0.55	2/0.790	4/0.603	11/0.744	39/0.812	4/0.792
0.55-0.60	3/0.705	2/0.627	15/0.802	41/0.802	8/0.797
0.60-0.65	4/0.668	2/0.593	17/0.723	31/0.759	11/0.785
0.65-0.70	3/0.823	3/0.630	25/0.746	65/0.749	6/0.745
0.85-0.90	16/0.516	5/0.526	41/0.514	110/0.521	22/0.632

$\lvert\cos\theta^*\rvert$	$N^{\gamma\gamma}_{data}/\varepsilon^{\gamma\gamma}$				
	195.5 GeV	199.5 GeV	201.6 GeV	205.7 GeV	206.3 GeV
0.05-0.10	8/0.769	11/0.738	7/0.766	23/0.703	3/0.804
0.10-0.15	12/0.770	6/0.733	6/0.723	20/0.816	9/0.729
0.15-0.20	24/0.717	11/0.794	4/0.733	16/0.700	4/0.913
0.20-0.25	5/0.844	13/0.848	6/0.875	31/0.794	12/0.888
0.25-0.30	8/0.749	15/0.746	5/0.826	17/0.803	6/0.902
0.30-0.35	7/0.751	13/0.747	7/0.734	20/0.750	14/0.833
0.35-0.40	15/0.763	15/0.677	5/0.769	28/0.709	4/0.493
0.40-0.45	11/0.716	18/0.676	7/0.625	24/0.776	13/0.654
0.45-0-50	18/0.834	20/0.802	9/0.802	17/0.784	7/0.877
0.50-0.55	29/0.792	20/0.738	7/0.749	32/0.766	9/0.806
0.55-0.60	20/0.792	25/0.781	11/0.799	35/0.804	14/0.788
0.60-0.65	25/0.775	21/0.718	11/0.759	33/0.728	11/0.746
0.65-0.70	27/0.723	16/0.758	10/0.764	66/0.755	16/0.746
0.85-0.90	76/0.645	67/0.651	32/0.667	122/0.657	32/0.628

Table 7: Number of data events within the range $|\cos\theta^*| \in [0.05, 0.70] \cup [0.85, 0.90]$, as a function of $|\cos\theta^*|$ and $\sqrt{s}$ and corresponding efficiencies (selection times trigger efficiencies corrected for the residual discrepancies between real data and simulation). The binning used was chosen in order to combine the data analysed by the four LEP collaborations.

$\lvert\cos\theta^*\rvert$	$d\sigma^0/d\Omega$ (pb/str)	$d\sigma^0_{QED}/d\Omega$ (pb/str)
0.0350-0.0855	0.50 ± 0.05 ± 0.02	0.55
0.0855-0.1360	0.56 ± 0.06 ± 0.02	0.56
0.1360-0.1865	0.69 ± 0.06 ± 0.02	0.57
0.1865-0.2370	0.63 ± 0.06 ± 0.03	0.59
0.2370-0.2875	0.60 ± 0.06 ± 0.02	0.62
0.2875-0.3380	0.62 ± 0.06 ± 0.02	0.66
0.3380-0.3885	0.74 ± 0.07 ± 0.02	0.71
0.3885-0.4390	0.72 ± 0.07 ± 0.02	0.77
0.4390-0.4895	0.70 ± 0.06 ± 0.02	0.84
0.4895-0.5400	0.92 ± 0.07 ± 0.02	0.93
0.5400-0.5905	1.01 ± 0.08 ± 0.02	1.05
0.5905-0.6410	1.15 ± 0.08 ± 0.02	1.21
0.6410-0.6860	1.39 ± 0.10 ± 0.03	1.40
0.6860-0.7310	1.59 ± 0.11 ± 0.03	1.64
0.8190-0.8625	2.95 ± 0.16 ± 0.05	3.18
0.8625-0.9060	4.50 ± 0.21 ± 0.08	4.48

Table 8: The differential cross-section for $e^+e^- \to \gamma\gamma$ with statistical and systematic uncertainties, obtained by combining the ten data sets, compared to the theoretical predictions from QED for each $\lvert\cos\theta^*\rvert$ interval. The displayed values correspond to an average centre-of-mass energy of 195.6 GeV and to a total integrated luminosity of 656.4 pb^{-1}.

$\sqrt{s}$ (GeV)	σ^0 (pb)	σ^0_{QED} (pb)	$\chi^2/ndof$
161.3	10.71 ± 1.42 ± 0.26	8.57	1.0
172.0	6.53 ± 1.14 ± 0.19	7.53	0.7
182.7	6.72 ± 0.45 ± 0.15	6.68	1.2
188.6	6.57 ± 0.25 ± 0.07	6.26	0.9
191.6	5.73 ± 0.57 ± 0.07	6.07	2.3
195.5	6.34 ± 0.34 ± 0.07	5.83	1.6
199.5	5.64 ± 0.31 ± 0.06	5.60	2.3
201.6	5.25 ± 0.43 ± 0.06	5.48	0.9
205.7	5.11 ± 0.21 ± 0.05	5.27	1.3
206.3	5.43 ± 0.38 ± 0.07	5.24	1.0
195.6	5.66 ± 0.11 ± 0.03	5.83	1.3

Table 9: The visible Born level cross-section (with statistical and systematic uncertainties) in the polar angle interval $\theta^* \in [25^\circ, 35^\circ] \cup [43^\circ, 88^\circ]$ and its complement with respect to 90 degrees (corresponding to $\lvert\cos\theta^*\rvert \in [0.035, 0.731] \cup [0.819, 0.906]$), for the ten data sets compared to the respective QED predictions and $\chi^2/ndof$ of the differential cross-section distributions with respect to the QED prediction. The visible cross-section corresponding to the combination of all data sets at an average centre-of-mass energy of 195.6 GeV and its respective theoretical prediction are also presented.

	ξ	$\xi^{+\sigma_+}_{-\sigma_-}$	Fit parameter	95% C.L. limits
QED cutoff	$\pm 1/\Lambda^4_\pm$	$-59.4^{+40.0}_{-39.0}$ TeV^{-4}	Λ_+	379 GeV
			Λ_-	300 GeV
Contact interactions	$1/\Lambda^4_6$	$-0.22^{+0.15}_{-0.14}$ TeV^{-4}	Λ_6	1537 GeV
	$1/\Lambda^6_7$	$-4.1^{+3.2}_{-3.1}$ TeV^{-6}	Λ_7	790 GeV
	$1/\Lambda^8_8$	$(-31 \pm 24)\ 10^{12}$ TeV^{-8}	Λ_8	21 GeV
e^* exchange	$1/M^4_{e^*}$	-142^{+104}_{-113} (TeV/c^2)$^{-4}$	M_{e^*}	295 GeV/c^2
Graviton exchange	λ/M^4_s	$1.36^{+0.92}_{-0.90}$ (TeV/c^2)$^{-4}$	$M_{s(\lambda=+1)}$	771 GeV/c^2
			$M_{s(\lambda=-1)}$	985 GeV/c^2

Table 10: Models predicting departures from QED and chosen estimators (ξ). The outputs of the likelihood function maximization are presented in the third column whereas the 95% C.L. lower limits on the free parameters of the models are presented in the fifth column. The value obtained for $\xi^{+\sigma_+}_{-\sigma_-}$ in case of the string mass scale corresponds to setting $|\lambda|$ to 1.

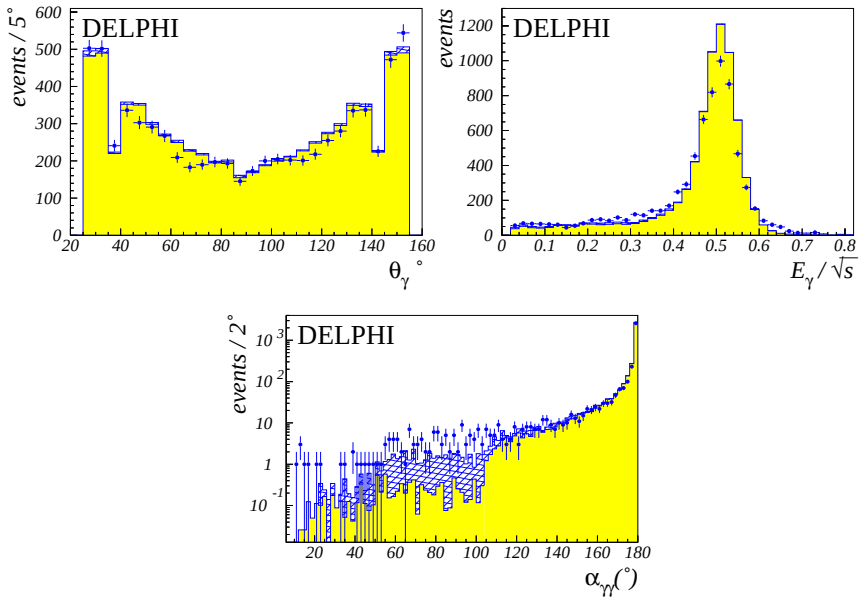

Figure 1: Distributions after the selection of multi-photonic events and before corrections for trigger and selection efficiency: of the polar angle of the two most energetic photons (top left); of their energy, normalised to $\sqrt{s}$ (top right) and of the angle between them (bottom) for the full data set (dots) compared to the SM predictions. The shaded histograms correspond to the $e^+e^- \to \gamma\gamma(\gamma)$ expectations while the hatched histograms correspond to the remaining processes: Bhabha and Compton scattering and $\nu\bar{\nu}\gamma\gamma$ events.

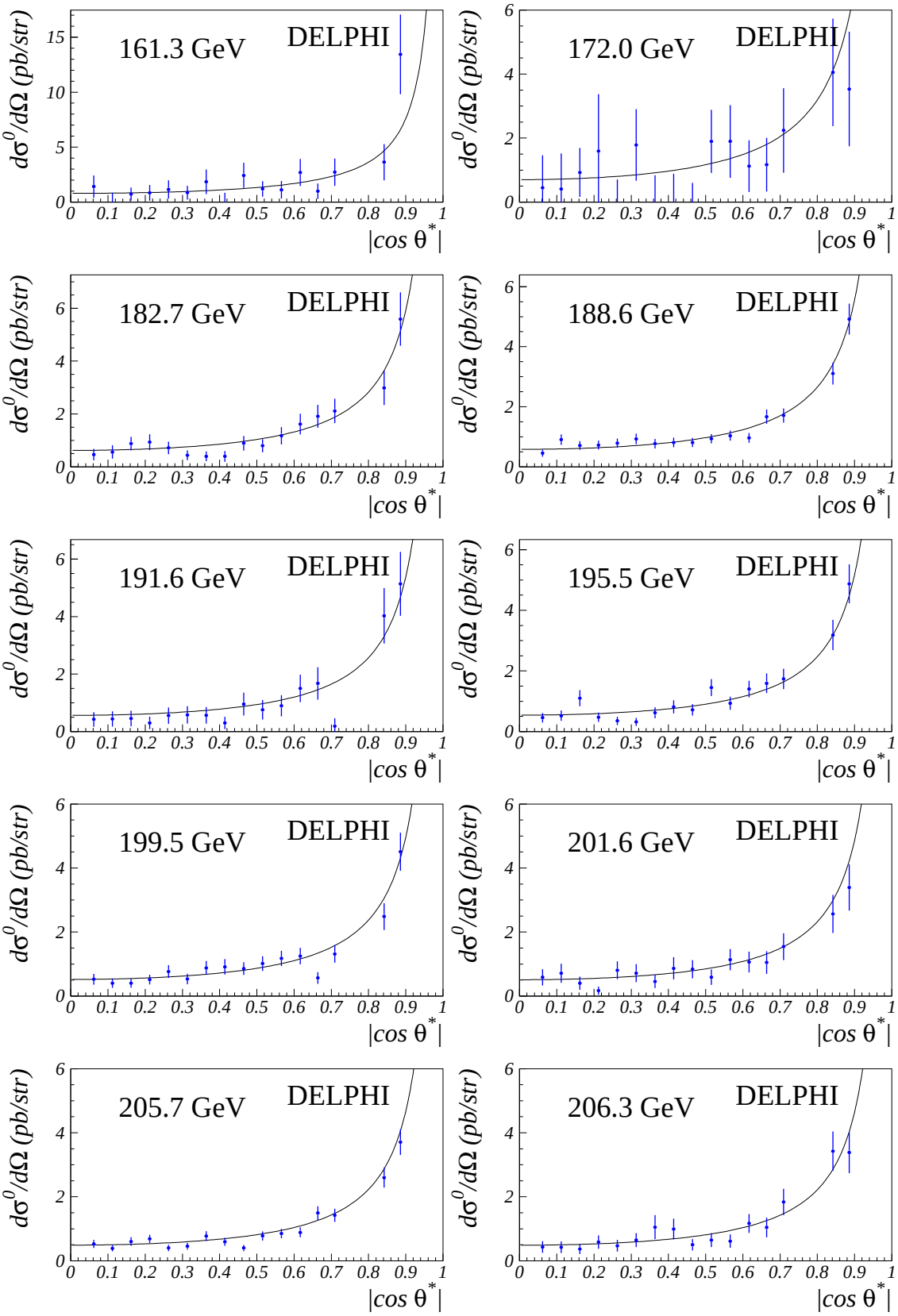

Figure 2: Differential Born level cross-sections obtained from the ten data sets, compared to the corresponding QED predictions. The error bars represent the statistical and systematic errors added in quadrature. Note the different scale used for displaying the 161.3 GeV data.

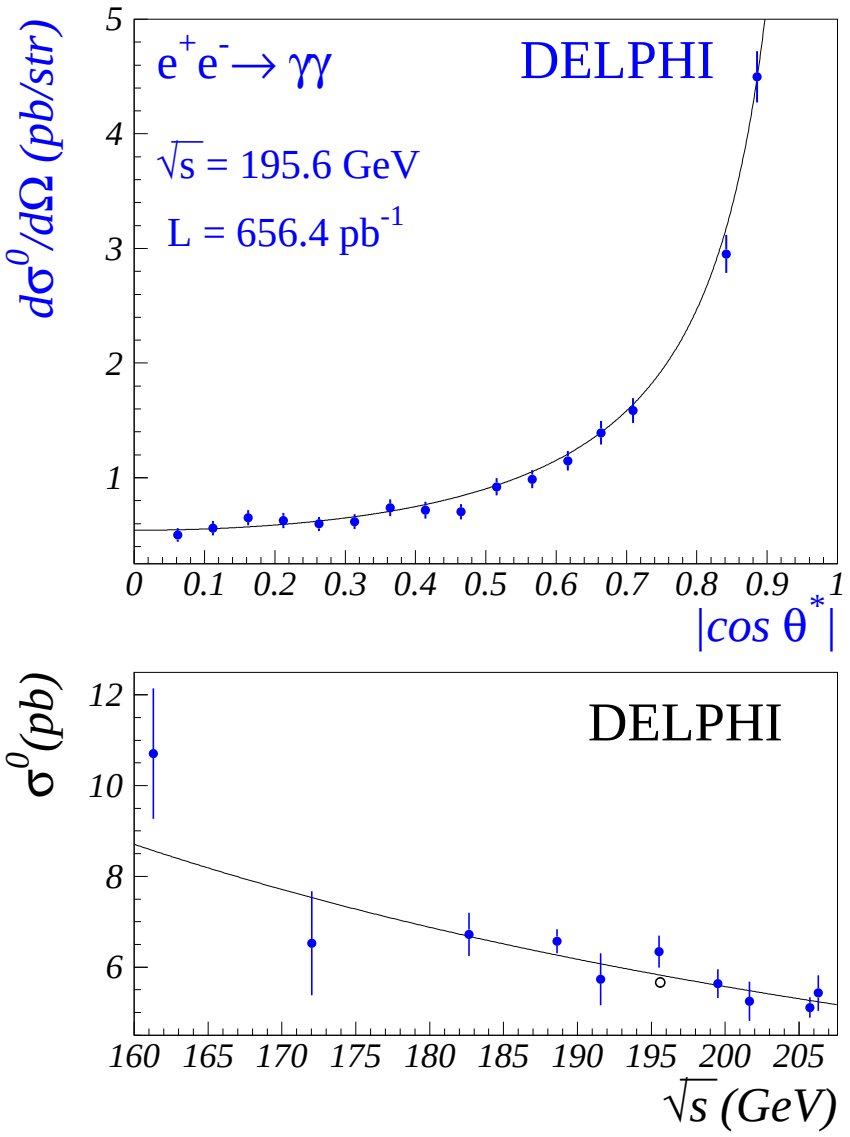

Figure 3: Top: The Born level differential cross-section for $e^+e^- \to \gamma\gamma(\gamma)$ obtained by combining the ten data sets at an effective centre-of-mass energy of 195.6 GeV (dots) compared to the QED theoretical distribution (full line). Bottom: The visible Born level cross-section for each of the ten data sets (dots) as a function of the centre-of-mass energy. The empty circle corresponds to the average visible Born cross-section for all LEP 2 data: 5.66±0.11±0.03 pb. The errors have been estimated by adding in quadrature the statistical and the systematic uncertainties associated to the measurements.

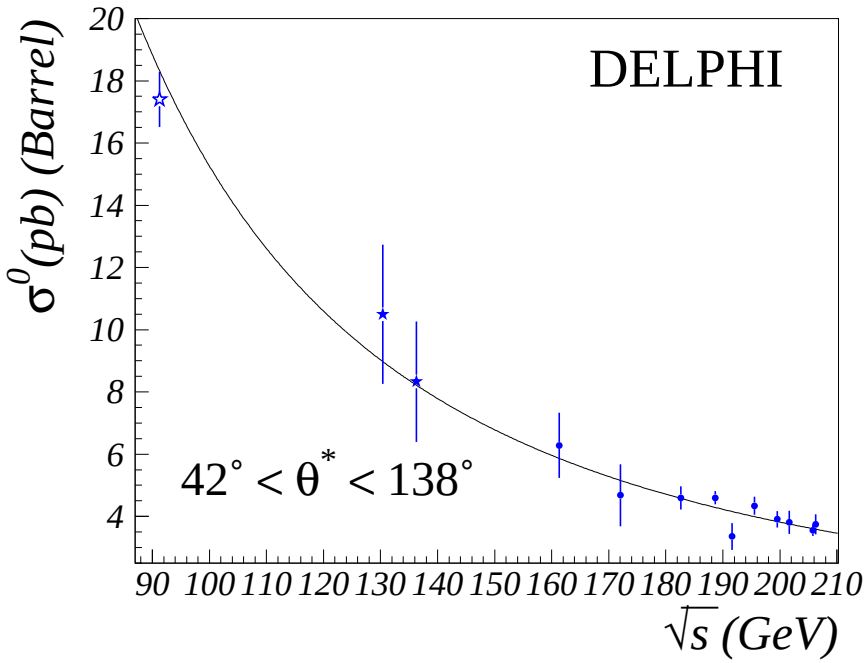

Figure 4: Born level cross-section for $e^+e^- \to \gamma\gamma$ in the barrel region of DELPHI, $42° < \theta^* < 138°$, as a function of the centre-of-mass energy, for 1990-1992 LEP 1 data (white star), LEP 1.5 data collected in 1995 and 1997 (black stars), and for LEP 2 data collected between 1996 and 2000 (dots), compared to the QED prediction. The errors have been estimated by adding in quadrature the statistical and the systematic uncertainties associated to the measurements.

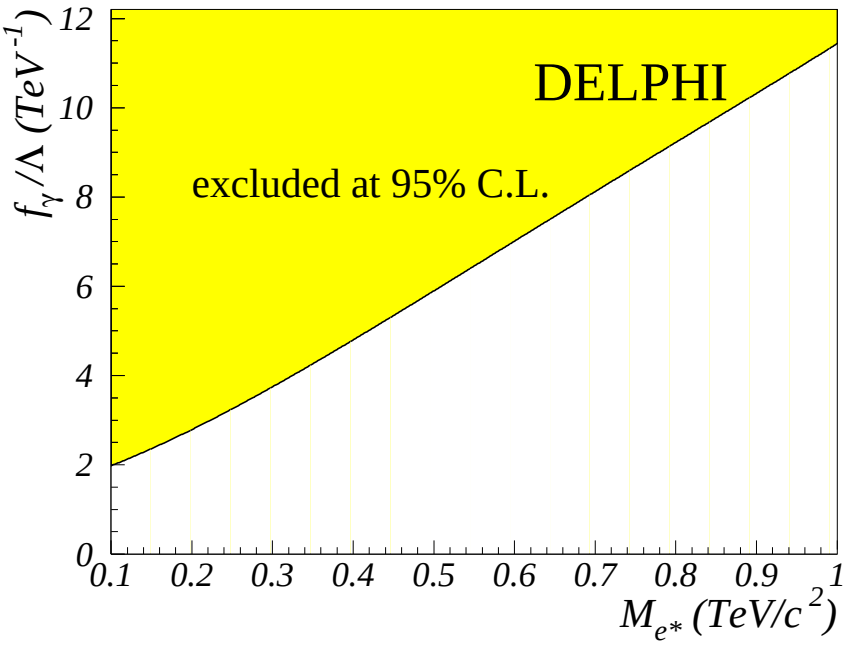

Figure 5: 95% C.L. upper bound on the coupling constant f/Λ (for $f_\gamma = f = f'$) as a function of the mass of an excited electron with a chiral magnetic coupling to the photon-electron pair.